



Advanced characterisation of thermo-mechanical fatigue mechanisms of different copper film systems for wafer metallizations



Stephan Bigl^{a,*}, Stefan Wurster^a, Megan J. Cordill^b, Daniel Kiener^a

^a Department of Materials Physics, Montanuniversität Leoben, Jahnstrasse 12, 8700 Leoben, Austria

^b Erich Schmid Institute of Materials Science, Austrian Academy of Sciences, Jahnstrasse 12, 8700 Leoben, Austria

ARTICLE INFO

Article history:

Received 14 December 2015

Received in revised form 26 April 2016

Accepted 26 May 2016

Available online 29 May 2016

Keywords:

Copper metallization

Thermo-mechanical fatigue

Twin boundary migration

Void formation

Surface roughening

Small angle grain boundary formation

Inorganic impurities

ABSTRACT

In this study, two different electrodeposited 5 μm thick copper films were subjected to thermal cycling. The microstructural evolution of both films was studied with a site specific tracking technique. It was observed that the initially similar microstructures develop differently upon cycling with respect to grain size and texture. In detail, a Cu film which contains residual inorganic species from the organic additives used during Cu plating, in the ppm regime, showed a constrained surface roughness evolution and marginal grain growth coupled with a stable twin boundary network. Furthermore, voiding in the film interior was observed. In comparison, a high-purity Cu film exhibited strong surface roughening in conjunction with pronounced grain growth promoted by twin boundary migration. Moreover, the film showed a (100) texture intensity increase as a result of strain energy minimization upon cycling and no void formation. These observations underline the influence of film processing related impurities on the thermo-mechanical behaviour of Cu thin films.

© 2016 Elsevier B.V. All rights reserved.

1. Introduction

In modern power semiconductor industry, increasing performance, efficiency and reliability are the driving forces for fundamental materials research and new product development. Semiconductor devices are composed of many different material layers, such as dielectric layers, intermetallic diffusion barriers and metallic films [1]. These film materials strongly differ regarding their intrinsic properties, for example, the elastic modulus and the coefficient of thermal expansion (CTE), as well as the structure, which can be crystalline or amorphous. For crystalline metal films, the grain orientations can be randomly distributed or strongly textured. Due to these different structures, the mechanical behaviour can range from strong to soft, or from brittle to ductile [2].

In power devices, extreme electric power densities create fast temperature rises resulting in large thermal stresses due to the CTE mismatch between the different materials. These thermal stresses lead to plastic deformation events, inevitably changing the microstructure of the films. Available literature illustrates that such repetitive thermo-mechanical loading processes cause degradation in the material stack in the form of void formation and crack nucleation, which might grow into the metallization layer or along an interface [3]. In a worst-case scenario, these fatigue defects induce local hot spots and a thermal runaway of the device, because the heat generated by a power pulse can no

longer be dissipated throughout the metallization layer. Hence, the integrity of metallizations for power devices plays a key role in the operational lifetime and reliability.

In advanced power semiconductor technology, copper is the material of choice for metallization. The outstanding electrical and thermal properties and its reduced susceptibility to electro-migration are a few of the many reasons why copper increasingly substitutes aluminium as a power metal [4,5]. The necessity of relatively thick metallizations (~5–20 μm) make electrochemical deposition the standard copper deposition process. The high degree of freedom of process parameters and the usage of additives lead to customized film microstructures.

However, electrodeposition processes can result in inorganic impurity levels after deposition and subsequent annealing steps due to the usage of additives in the electrolyte. Such impurity levels can make up trace amounts, or reach up parts per million (ppm) concentration levels, altering the initial microstructure and surface morphology [6]. Previous studies showed that even trace quantities of inorganic impurity levels have a severe influence on the mechanical behaviour of the films [7,8], while early research using pure, sputtered Cu films did not study the influence of impurities on the thermo-mechanical behaviour [5,9,10]. Therefore, the connection between inorganic impurity levels of electrodeposited films and the corresponding thermo-mechanical behaviour is of great importance, since electrodeposition represents the current industry standard.

In the literature, many different studies report the fatigue behaviour of copper films [11–15]. Such studies often show experimental

* Corresponding author.

E-mail address: stephan-paul.bigl@stud.unileoben.ac.at (S. Bigl).

restrictions, such as free standing copper films [8,16], or pure mechanical cyclic testing [17–19]. Hence, results are not applicable for Cu metallizations used in semiconductor devices since plastic deformation is always achieved by a combination of thermal activation (thermal energy) and applied stress (mechanical energy) [20]. These previous investigations concluded that fatigue damage evolution of copper films is strongly dependent on film thickness and grain size [13], as well as crystal orientation of the grain [12]. The fatigue events are observed as surface roughening and extrusions formed on the film surface [14]. Furthermore, it is assumed that twin boundaries play a major role regarding the plastic deformation that acts as a non-regenerative dislocation source [21], and could serve as sites for void nucleation. Most of these studies do not resolve the on-going mechanisms throughout the fatigue experiment, hence making interpretation of results difficult. Therefore, the understanding of microstructural changes with respect to the remaining impurities in the copper layers upon cyclic thermo-mechanical loading is of fundamental importance to predict and improve lifetime and reliability of microelectronic devices.

In this work, experimental results of two different thermo-mechanically fatigued electrodeposited copper films are presented. One film system (Film A) was designed to contain relatively high amounts of inorganic impurities (mostly sulphur and chlorine), while the second film system (Film B) was processed resulting in a significantly lower amount of inorganic impurities. The experimental evaluation of the fatigue mechanism(s) was performed, using a site specific tracking technique [22]. Microstructural evolution was investigated by combining topographical information using atomic force microscopy (AFM) and crystallographic information with electron backscatter diffraction (EBSD) throughout the thermal fatigue experiment. This enabled the study of global structural parameters like roughness, average grain size and grain boundary characteristics, as well as investigate distinct microstructural features displaying twin grain boundary migration, grain growth, and diffusional mass transport along certain grain boundaries, throughout the thermo-mechanical loading experiment. The observations were then critically evaluated regarding the influence of inorganic impurities on the microstructural evolution.

2. Materials

For all of the presented data, 5 μm thick electrochemically deposited polycrystalline copper films were used. The two copper film systems were deposited on 725 μm thick silicon wafers of (100) orientation. As a diffusion barrier, a few nanometers thick tungsten-based layer was used followed by a 300 nm Cu seedlayer. After electrodeposition, a 30 min annealing step at 400 °C in an inert atmosphere was performed to ensure a room temperature stable microstructure. Film A was designed to result in a copper film with a high remaining inorganic impurity content (≤ 100 at ppm), and Film B resulted in an almost impurity-free copper film. For more details see [7].

3. Experimental

For an experimental imitation of the thermo-mechanical load in the copper films induced by the high power density in semiconductor devices, the samples were thermally cycled in an infrared furnace (IRF 10, Behr GmbH, Düsseldorf, Germany). The specimens were cut from a 200 mm wafer measuring about 5 mm \times 10 mm and heated indirectly via strong quartz lamps in customized sample carriers. Using K type thermocouples brazed onto extra samples, the film temperature during the programmed temperature cycle was monitored. All specimens in this publication were subjected to thermal cycles between 170 °C and 400 °C to mimic realistic temperatures [3]. This results in a total applied strain due to the CTE mismatch per cycle of about 0.7% when using the average CTE values for Cu and Si in the corresponding temperature range [23,24].

The basic thermo-mechanical characterisation of both films was performed using a wafer curvature system for in-situ film stress characterisation up to 1000 °C [25]. With a multiple optical beam sensor, kSA MOS (k-Space Associates, Inc. Dexter, 48130 USA) the film stress evolution was measured between room temperature and 400 °C using a heating and cooling rate of 10 °C/min.

Fig. 1 shows a direct comparison of the time–temperature relation between a conventional wafer curvature experiment using a heating rate of 10 °C/min and the programmed thermal cycle in the infrared furnace (IRF) for the desired temperature range of 170–400 °C. Thereby, 30 cycles are achieved in the IRF, whereas in the same time span only one thermal cycle is performed in the wafer curvature, indicating accelerated fatigue testing with respect to testing time. One thermal cycle corresponds to an average heating rate of 17 °C/s (from 170 °C to 400 °C) and 3 °C/s cooling rate (from 400 °C to 170 °C) with a total cycle time of about 95 s. During the cycling process in the IRF a constant gas flow of N_2/H_2 (95 vol% N_2) gas mixture of ~ 1 l/min through a quartz tube containing the specimens was used to minimize oxidation of the copper surface.

For thermal fatigue investigations of the copper films during the cycling process a surface area-specific tracking technique was used. A representative surface area was marked with orientation indents (Vickers micro indents HV 0.02 & HV 0.05), to ensure the tracking of the identical film area throughout the whole experiment. The investigations were performed regarding microstructural evolution using EBSD and topographical evolution using AFM. A more detailed description of the applied technique and its features can be found in [22].

Using a Dimension 3100 AFM (Bruker Inc., Billerica, USA) and a scanning electron microscope (SEM) LEO 1525 (Zeiss Inc., Oberkochen, Germany) for EBSD analysis, specimens were examined throughout the thermal cycling process. AFM height images were between 30 \times 30 μm^2 and 50 \times 50 μm^2 in size with a scan resolution of 512 lines. AFM post image analysis was performed using Gwyddion 2.36 software [26]. The EBSD scans resulted in a scan size between 100 \times 100 μm^2 and 150 \times 150 μm^2 , using a step size of 0.2–0.3 μm . The EBSD scanned area incorporated the AFM scanned area. For all EBSD scans 20 kV acceleration voltage and 120 μm aperture size were used. EBSD data analysis was performed using TSL OIM Analysis 5 software. For correct grain definition, identified pixels had a 15° tolerance angle and a minimum grain size of 3 pixels. For the presented inverse pole figure (IPF) images, overlaid with the image quality (IQ), a confidence index clean-up with a threshold value of 0.07 was performed. To reveal through-thickness fatigue mechanisms, film cross-sections were prepared using dual beam focused ion beam (FIB) workstations, either with a LEO 1540 (Zeiss Inc., Oberkochen, Germany) or an Auriga SEM equipped with Cu ion FIB (Zeiss Inc., Oberkochen, Germany). After

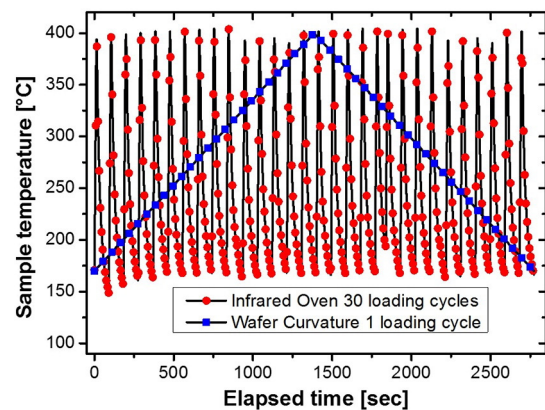


Fig. 1. Comparison of the sample temperature–time response in a conventional wafer curvature experiment and the fast thermal cycling in an infrared furnace between 170 °C and 400 °C.

cutting a large trench with an ion current of 20 nA, subsequent fine polishing steps with 1 nA and 100 pA produced a good quality for cross-section imaging of the cycled copper films. To maintain the surface quality needed for AFM and EBSD characterisation after several thousand thermal cycles, the specimens were treated with acetic acid after thermal cycling. Samples were put into a 100 vol% acetic acid at 35–40 °C for ~3 min, which selectively etches copper oxide and does not affect the actual copper surface [27].

4. Results

4.1. Initial film microstructure

Fig. 2 displays the initial microstructure of the two film systems. The $50 \times 50 \mu\text{m}$ IPF-IQ images reveal the microstructural characteristics of the two films. The IPF standard triangle, used for every EBSD image in this work, can be found in Fig. 6d. For better illustration of the microstructure white lines (excluding $\Sigma 3$ and $\Sigma 9$) in Fig. 2 indicate high angle grain boundaries (HAGB, $>15^\circ$), whereas black lines indicate primary (coherent and incoherent) twin boundaries ($\Sigma 3$). In both samples, low angle grain boundaries (red lines) and secondary twin boundaries (grey lines, $\Sigma 9$) make up a negligible contribution to the total grain boundary characteristics.

Both film systems reveal a polycrystalline microstructure where the grains possess a significant portion of twin boundaries. The main microstructural distinction is that Film A has a higher initial fraction of twins than Film B, which can be also seen through the entire film thickness (Fig. 2c, d). The average initial grain size, including the twin boundaries resulted in $2.8 \pm 0.9 \mu\text{m}$ for Film A and $3.2 \pm 1.1 \mu\text{m}$ for Film B. Concerning the texture, both sample types reveal an almost randomly orientated polycrystalline microstructure with no preferable crystal orientation. Using the elastic constants of the stiffness tensor for copper (c_{11} : 168.4 GPa, c_{12} : 121.4 GPa, c_{44} : 75.4 GPa) [28] the elastic modulus distribution and the mean elastic modulus of the initial scanned surface area was determined using the OIM Analysis software. The calculated elastic modulus is 110 ± 31 GPa for Film A and 112 ± 30 GPa for Film B. For determining the elastic modulus of absolutely randomly oriented copper, being equivalent to texture-less polycrystalline copper, a custom EBSD scan file was generated and analysed, where the result for the average Young's modulus was 109 GPa.

4.2. Basic thermo-mechanical behaviour

To evaluate the basic thermo-mechanical behaviour of the two sample types, film stresses were measured with wafer curvature. Fig. 3 shows the stress vs. temperature evolution of Films A and B. The first cycle (starting from room temperature) and second cycle (80–400 °C) are plotted in comparison to the stress behaviour of the same samples after being exposed to 80 thermal cycles between 170 °C and 400 °C in the IRF. It can be seen that the evolving stresses in the initial cycle differ strongly between Films A and B. Film A (Fig. 3a) shows a very pronounced linear elastic behaviour between room temperature and about 100 °C, whereas Film B (Fig. 3b) deviates from a pure elastic behaviour around 75 °C. This can also be seen in the stress evolution at higher temperature, where Film B stresses relax at temperatures around 200 °C, compared to about 250 °C in Film A. Overall, Film A thermo-mechanically behaves stiffer (steeper thermo-elastic slope) and stronger (higher tensile flow stress) compared to the more compliant and softer Film B.

The same behaviour can be observed in the second cycle starting from 80 °C. Treating the initial linear stress decrease as a pure elastic phenomenon due to the thermal expansion mismatch between Cu and Si, the stress slope $d\sigma_f/dT$ can be described as following [29]:

$$\frac{d\sigma_f}{dT} = \left[\frac{E_f}{(1-\nu_f)} \right] * (\alpha_s - \alpha_f). \quad (1)$$

The stress slope is the product between the biaxial modulus of the film, where E_f denotes elastic modulus and ν_f the Poisson's ratio of the film, and the expansion mismatch between the substrate α_s and the film α_f . Determining the thermo-elastic slope for both samples between 90 and 110 °C, Film A results in -2.49 MPa/°C and Film B in -2.09 MPa/°C. Using the elastic moduli for A and B determined from the EBSD, the average CTE value of 3.28 ppm/K for silicon in the corresponding temperature range and 0.35 as the Poisson's ratio for polycrystalline copper, results in CTE values for Cu of 17.8 ppm/K and 15.3 ppm/K for Films A and B [24,28]. Film A displays an almost perfect correlation to literature data of measured thermal expansion, which is ~17.4 ppm/K in the corresponding temperature region [23]. Film B results in a lower equivalent CTE value and deviates from the literature bulk value.

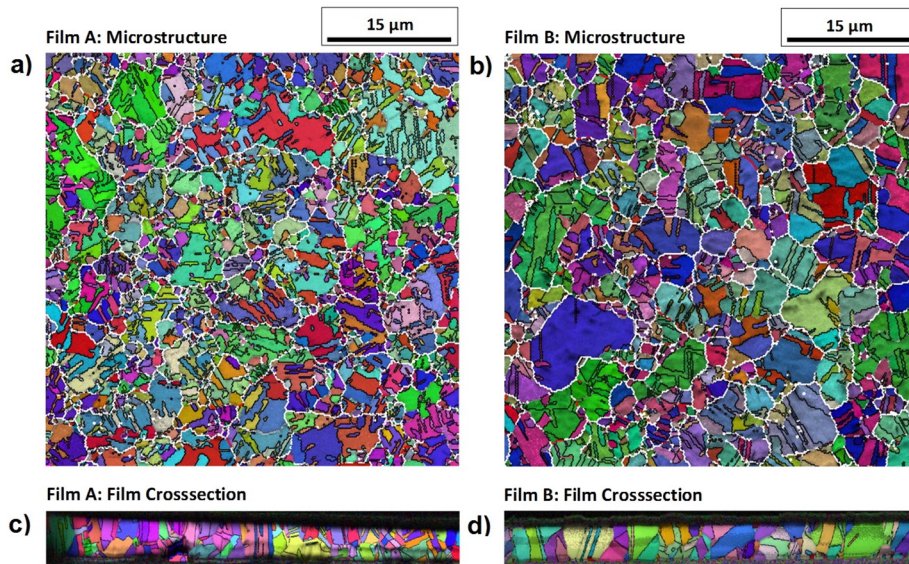


Fig. 2. Initial surface microstructure of Film A (a) and B (b), where grain boundaries (white lines) and twins (black lines) are indicated. (c–d) Cross-sectional microstructure, where only twins are indicated (black lines).

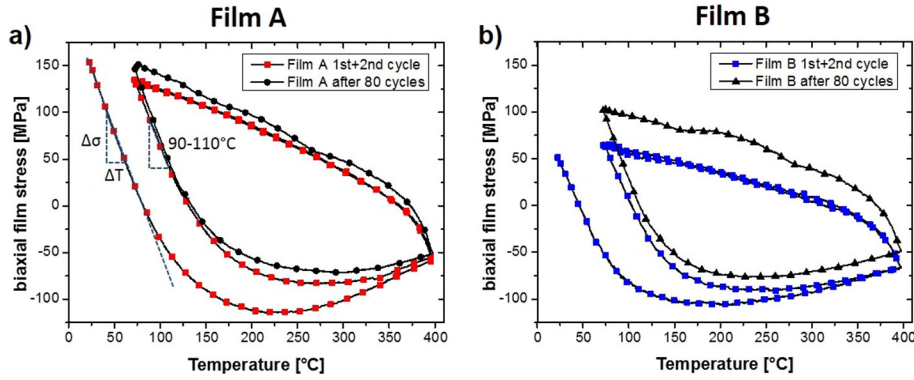


Fig. 3. Basic thermo-mechanical behaviour of (a) Film A and (b) Film B between room temperature and 400 °C.

A clearer picture of the CTE can be obtained when Films A and B are compared after 80 thermal cycles in the IRF. Fig. 3 indicates that in both film systems the stress hysteresis is shifted towards the tensile stress state. Besides this shift, the elasto-plastic behaviour of Film A itself remained unchanged, but for Film B the thermo-mechanical behaviour changes as function of cycle number. The elastic regime becomes more pronounced, which can be seen in the initial heating and cooling after reaching 400 °C in the 80th cycle, indicating that the stress-temperature evolution in Film B approaches that of Film A. This is also found in the thermo-elastic behaviour, where the slope of Film B between 90 and 110 °C results in $-2.51 \text{ MPa}/^\circ\text{C}$ compared to $-2.63 \text{ MPa}/^\circ\text{C}$ for Film A. Hence, the obtained wafer curvature results of the two film systems indicate that Films A and B exhibit a different global thermo-mechanical behaviour, although starting with very similar initial microstructures. Therefore, there is a need for a closer look during the cycling to illustrate the on-going microstructural changes, which will enable the classification of the present fatigue mechanisms in the two film systems.

4.3. Global data on microstructural evolution

For the global characterisation of the copper film evolution, the grain size, including the twins as grain boundaries, the fractional twin boundary length, the root mean square (RMS) surface roughness and the normalized texture intensity in the (100) out of plane crystal direction, were examined between the initial stage and 3500 thermal cycles.

In Fig. 4a and b, a direct comparison of the two film systems regarding their grain structure development can be found. The grain diameter (with corresponding standard deviation) is very similar at the beginning, however, the grain size evolution throughout cycling significantly deviates. Film A shows a slight increase of the grain size. Starting from $2.8 \pm 0.9 \mu\text{m}$, the grain size increased up to $3.9 \pm 1.2 \mu\text{m}$ after 3500 thermal cycles. In Film B, significant grain growth can be observed in the initial 1000 cycles, increasing the grain diameter from $3.2 \pm 1.1 \mu\text{m}$ up to $5.1 \pm 1.7 \mu\text{m}$. Further cycling led to a final grain size of $5.8 \pm 1.9 \mu\text{m}$ after 3500 cycles.

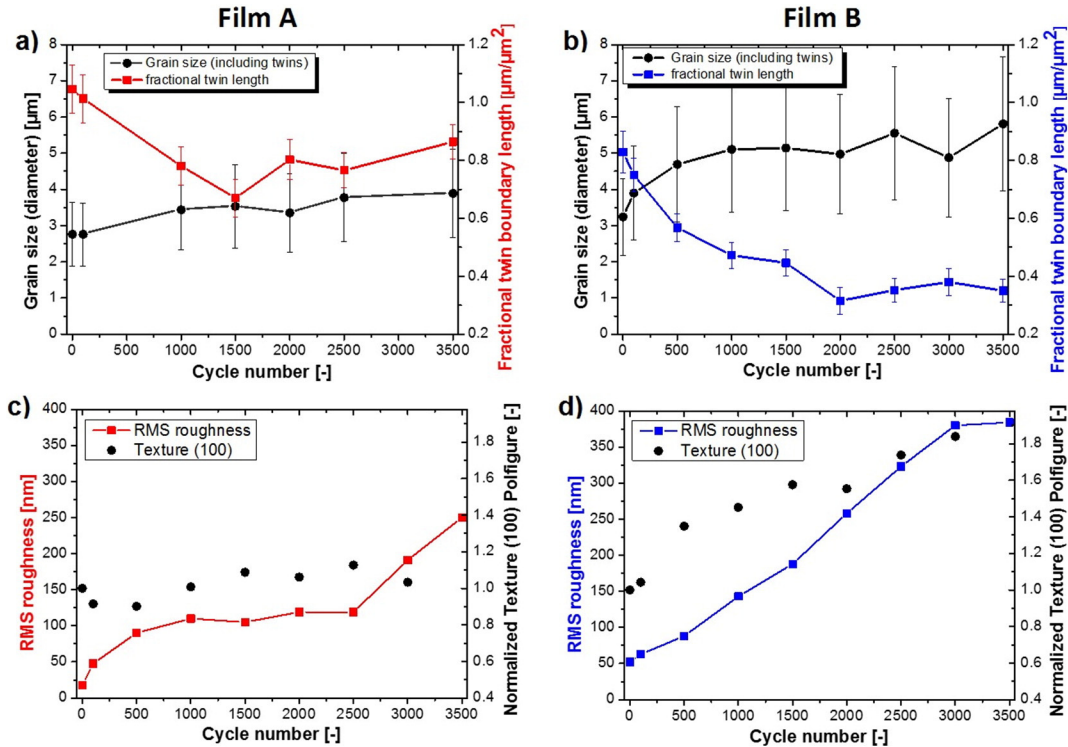


Fig. 4. (a, b) Grain size and fractional twin boundary length evolution for Film A and Film B as a function of cycle number. (c, d) Surface roughness development and evolution of the (100) texture intensity for Film A and Film B, respectively.

The evolution of the fractional twin boundary length (including measurement uncertainty) is also presented in Fig. 4a, b, where the total measured twin boundary length is divided by the total scan area. This gives a quantitative parameter regarding the twin boundary evolution and can be used to evaluate the on-going plastic deformation. For example, Film A started with about $1.05 \pm 0.08 \mu\text{m}^{-1}$ fractional twin length which decreased to $0.78 \pm 0.07 \mu\text{m}^{-1}$ in the first 1000 cycles. This indicates a diminishing of twin boundaries, while the following 2500 cycles show a relatively stable twin boundary length resulting in $0.86 \pm 0.06 \mu\text{m}^{-1}$ final fractional length. Film B reveals an approximately 26% lower initial fractional twin boundary length of $0.83 \pm 0.07 \mu\text{m}^{-1}$, which can be also seen qualitatively in Fig. 2. The fractional twin length strongly decreased to $0.57 \pm 0.05 \mu\text{m}^{-1}$ after 1000 cycles and is further reduced to a final fractional length of $0.35 \pm 0.04 \mu\text{m}^{-1}$ after 3500 cycles. In direct comparison, the two film systems reveal quite different microstructural evolution. Film B shows an almost 100% increase of the average grain diameter, which is due to a continuous decrease of twin boundaries by more than a factor of two after 3500 cycles. On the contrary, Film A exhibits an increase of the grain size of only 40% and the initially decreasing twin boundary length remains constant after ~1000 cycles.

Fig. 4c–d present the topographical evolution, given by the RMS surface roughness and the texture evolution of the (100)-texture. The RMS roughness gives a quantitative parameter in regards to the height evolution due to mass transport or deformation event. The (100) texture was chosen because grains with a low biaxial modulus are preferred to grow in order to minimize the strain energy, thus giving an orientation-specific driving force which could influence the texture evolution [30]. The (100)-texture is presented perpendicular to the loading direction, since the thermo-mechanical loading generates stresses in the in-plane direction of the copper films.

Film A starts with an initially flat surface of ~17 nm RMS roughness, which increases up to ~100 nm after 1000 cycles. The surface roughening is then continued through cycling up to 250 nm, although with not much change between 1000 and 2500 cycles. Film B starts with an initially wavier surface of ~52 nm RMS roughness, which linearly increases throughout the fatigue experiment up to 384 nm. Both film systems show that throughout the cycling severe surface roughening occurs. Nevertheless, Film B has a 50% rougher surface than Film A, indicating that more plastic deformation can be observed on the free film surface.

With respect to texture evolution, the analysis was performed identically for both film systems. The texture intensity regarding the (100)-texture was determined using the technique of series expansion of generalized spherical harmonics, a tool which is incorporated in the OIM software. All scans were analysed using 16 as the order of series expansion and 5° as the Gaussian half-width, a parameter for smoothing the texture plot. The obtained maximum intensity values (equivalent to a statistical probability) for each cycling stage were then normalized with regard to the value of the initial microstructure. There, Film A had 2.4, as absolute (100)-texture intensity and Film B 1.6. Film A reveals no change of the intensity of the (100)-texture throughout the cycling. In the case of Film B, the intensity of the out of plane orientation increased by a factor of 1.8, demonstrating that the thermo-mechanical loading leads to a texture change in the film.

4.4. Local microstructural evolution – early stage

Because of the global changes seen in Fig. 4, a more specific and local investigation of the fatigue evolution is necessary. This would enable a correct interpretation of the presented global results, revealing the microstructural mechanism on the local scale for Films A and B. Since excessive changes were observed in the first 1000 cycles, Fig. 5 shows the combination of EBSD (Fig. 5a–c) and AFM (Fig. 5d–f) images of Film A for 0, 500 and 1000 cycles. Additionally, three height profiles (Fig. 5g–i) are shown to reveal the height evolution for certain microstructural features. It should be pointed out that slight colour changes

can be observed from one to another cycle stage in the EBSD image. This is due to the fact that even minor changes in the sample-detector alignment upon sample mounting can have an impact on the colour appearance of the grains. In the initial film topography (Fig. 5d) Film A exhibits a very flat surface with pronounced grooves at high angle grain boundaries, as well as grooves at the twinned interfaces. The corresponding EBSD image (Fig. 5a) shows that the initial microstructure is composed of fine grains with a strongly twinned substructure (black lines). Therefore, many grains consist of multiple twin configurations, indicating that more than one parent/twin configuration is present. The topographical evolution shows that after 500 cycles (Fig. 5e) sharp elevations at the grain boundaries formed, as well as distinct uprising of grains, which are further evolving in the subsequent cycles (Fig. 5f). For example Profile 1 (Fig. 5g) displays the uprise of two small twinned grains. After 1000 cycles, the two grains show a 250 nm difference in height compared to the surrounding grains. Profile 2 (Fig. 5h) presents the interface evolution between neighbouring grains. In the three profiles, it can be seen that starting from a flat surface (0 cycles) with some grooves at the grain boundaries (purple line), severe hillocks formed. These pronounced walls rise up to about 400 nm after 1000 cycles. From the AFM images and the profile sections it can also be observed that mass transport of the in-between lying approximate (100)/(212)-twinned grain to the neighbouring grains forms these hillock-like features. Furthermore, the profile sections indicate that grain growth in Film A is hindered. It can be seen that the positions of evolving features do not change throughout the cycling process. In Profile 3 (Fig. 5i), the topographical evolution between small grains can be observed. A large height gain evolves between two grains sharing a small angle grain boundary (position at $6 \mu\text{m}$ in Profile 3). It can be seen that deep grain boundary grooves develop due to diffusional mass transport from one grain to another grain. Notably, in all profiles no significant topographical evolution between 500 and 1000 cycles was observed. This is in accordance with the global RMS roughness evolution shown in Fig. 4c.

For a more detailed interpretation of the microstructural changes of Film A during the initial thermo-mechanical loading process, Fig. 6 presents a more localized depiction of the microstructural evolution of Film A between 0 and 1000 cycles. As a result of the increasing roughness formed at grain boundaries and growing grains in the out of plane direction, fewer points can be identified in the EBSD scanning in the later stage. This results in black areas due to the overlaid image quality and is present in all scans that do not display the initial microstructure. Despite the moderate grain growth and greater microstructural stability in Film A, certain crystallographic mechanisms can be identified. Therefore, five distinct microstructural features are labelled with numbers in the in the EBSD images (Fig. 6a–c) to indicate these mechanisms in the early stage of fatigue (0–1000 cycles).

It can be seen that grain growth is achieved by certain twin/parent configurations in Film A. Grain growth is achieved via twin boundary migration (Feature 3), twinning/detwinning (Feature 2, 5), as well as distinct formation of new twin configurations (Feature 1). Additionally, localized roughening in the form of the uprise of Feature 1 can be observed, as identified in Fig. 5e–f. The majority of grains show insignificant microstructural changes (Feature 4), where no microstructural changes occur, especially comparing 500 and 1000 cycles.

Fig. 7 highlights the site specific microstructural changes in the first 1000 thermal cycles of Film B. As for Film A, the crystallographic evolution (Fig. 7a–c) is matched by the topographical evolution (Fig. 7d–f) for 0, 500 and 1000 loading cycles. Three profile sections indicate the topographical evolution of distinct microstructural features as shown in Fig. 7g–i. Additionally, four selected features are marked in the intermediate cycling stage (Fig. 7b), used to describe the on-going microstructural changes in detail. The initial microstructure for Film B consists of small grains composed of many different twin configurations, similar to Film A. The deposition process resulted in a wavier and rougher film surface. From a film morphology point of view, the

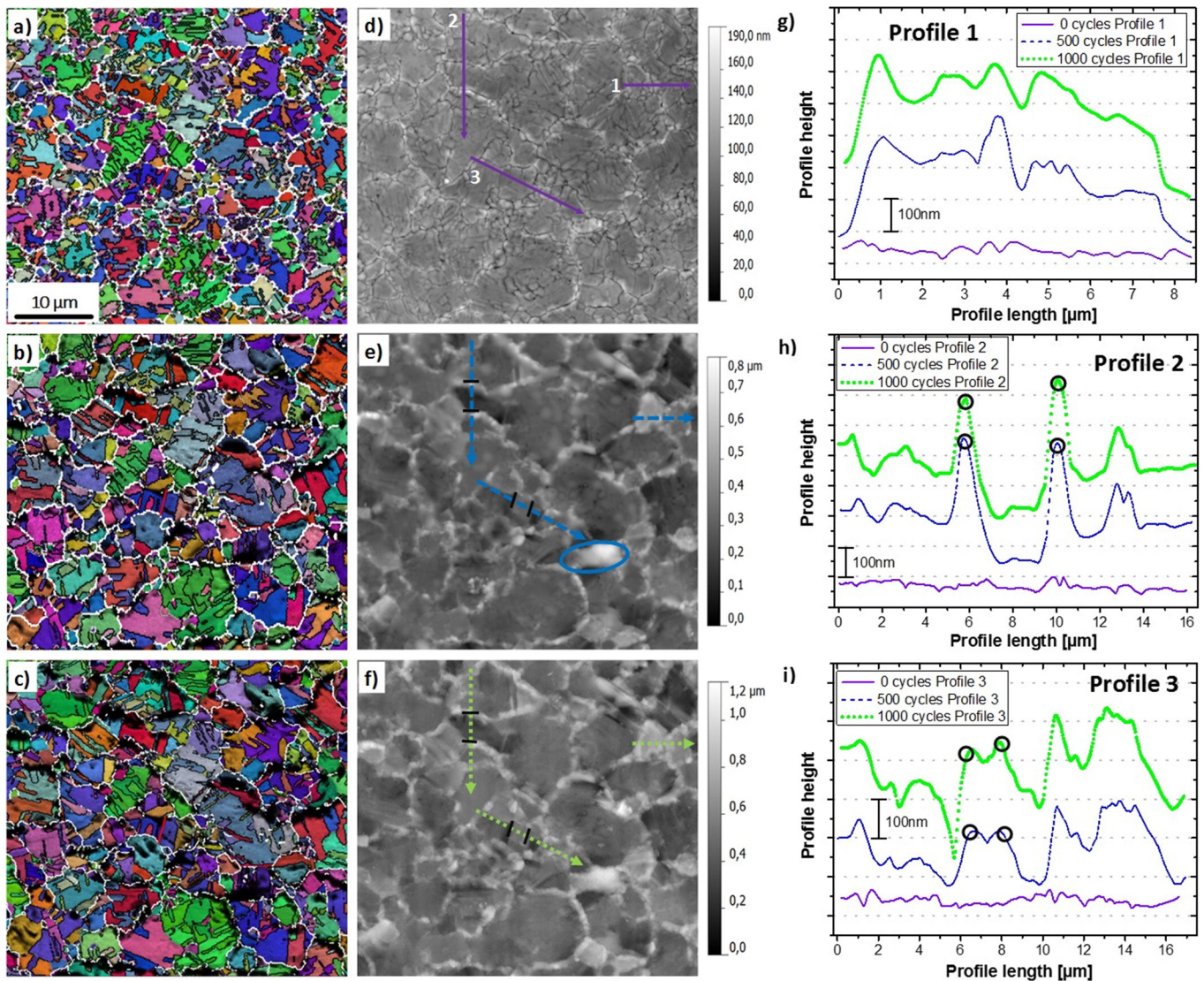


Fig. 5. Early site specific microstructural evolution of Film A. Crystallographic evolution (a–c) is matched by the topographical evolution (d–f) of the same surface area for 0, 500 and 1000 cycles. Additionally, three selected microstructural features are examined regarding their topographical evolution, indicated by Profiles 1–3 (g–i).

grains with high angle boundaries reveal grooves at the interfaces, which are matched with the boundaries (white lines) in the EBSD section (Fig. 7a), although the twinned regions in Film B do not show such pronounced grooves as seen in Film A. As indicated in the topographical evolution of Profile 1, grain growth is active throughout the thermo-mechanical cycling, as the distance between the peaks of the walls increases. By examining the profile section at the HAGB interface, it can be seen that the particular grain is growing continuously. A distinct uprise of the grain interface can be observed, although surface roughening is also occurring within the grain. Profile 2 highlights the uprise and growth of a small lamella twinned grain. After 1000 cycles the grain shows a distinct uprise of about 400 nm. Profile 3 displays the height evolution of several neighbouring small twinned grains. The profiles indicate that during the cycling the region is laterally shrinking, but a significant height evolution is observed. Therefore, the severe roughening occurs at twin boundary interfaces and high angle grain boundaries which form deep valleys upon cycling.

In general, it can be stated that the film surface evolution for Film B leads to a rougher topography after 1000 cycles, which was already seen by the global RMS roughness evolution in Fig. 4. It can be seen that the roughening in Film B is distinctively different from Film A, where the height evolution occurred at very confined regions such as high angle

grain boundaries (see Fig. 5d–i). In Film B, the roughening is not restricted to certain areas. Furthermore, grain growth can be quantitatively observed with AFM, indicating that HAGB are mobile and not hindered by certain mechanisms as seen in Film A. To classify the microstructural changes in Film B, four distinct features are indicated in the EBSD images (Fig. 7a–c). In the first 500 cycles the majority of grains exhibited a significant reduction of the twin boundary length via twin boundary migration. This can be observed in Features 1, 3 and 4. The approximately (212) oriented twinned grain (Feature 1) forms a stable parent/twin structure after losing a significant portion of twin boundary length in the first 500 cycles. A similar development is seen for Feature 4 where internal twins and small twin lamellae diminish, forming a stable twin/parent configuration (Fig. 7b). In case of Feature 3, the multiple twinned grain, the first 500 loading cycles lead to a twin-free (112) oriented grain. To accommodate the externally applied thermo-mechanical load grains not only plastically deform via twin boundary migration, but also with normal grain growth via HAGB migration. This can be seen for Feature 1, where Profile 1 reveals the grain growth in the first 1000 cycles (Fig. 7g). For Feature 2 the significant grain growth is along with the formation of two parallel twin lamellae by the expense of smaller grains (Fig. 7b). Further thermal loading up to 1000 cycles (Fig. 7c) indicates that the above mentioned

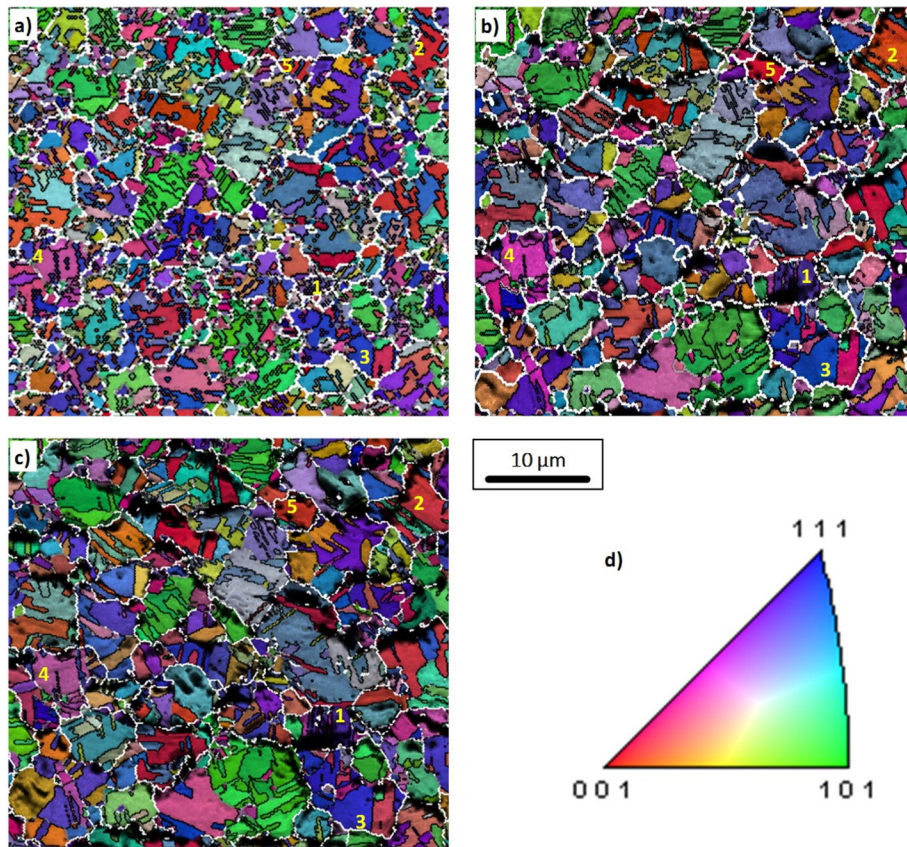


Fig. 6. Microstructural evolution of Film A. The IPF images overlaid with the image quality display the changes in respect to the cycling stage of 0, 500 and 1000 thermal cycles (a–c). Five distinct microstructural feature are highlighted to describe the changes in Film A during thermo-mechanical loads in (b). See text for details.

microstructural changes are still occurring although in a less pronounced manner. Additionally, it can be seen that, once a stable microstructural configuration is formed (e.g. parent/twin substructure) processes such as faceting between certain boundaries as well as within coherent crystal regions can be observed. Such an example is indicated in Feature 2, where severe faceting between the (111)/(115)-oriented parent/twin region can be observed as well as a distinct uprise of the (115)-oriented twin region at the very top (Fig. 7e–f). Moreover, the microstructure in Film B exhibits a pronounced surface roughening within the grains, indicated by the black spots, due to the overlaid IQ (Fig. 7c).

4.5. Local microstructural evolution – advanced stage

In the progressed cycling stage microstructural phenomena, such as twin boundary migration or normal grain growth, do not change very much, making a direct examination of the local changes essential. Fig. 8 represents the microstructural changes for Film A on a local scale in the advanced state. A $(30 \times 30) \mu\text{m}^2$ sample surface section is matched after 1500 cycles (Fig. 8a, c) and 3500 cycles (Fig. 8b, d) with respect to the crystallographic (EBSD) and topographical (AFM) changes. For further information two profile sections are used to indicate topographical changes of certain features (Fig. 8e, f), and FIB-prepared trenches reveal the cross-section after 3500 cycles (Fig. 8g, h). It should be pointed out that for the ease of indication, in both cycle stages only twin boundaries were indicated with black lines in the EBSD image.

From a topographical point of view, it can be stated that the surface morphology of Film A appears in a defined manner after 1500 cycles. Certain, especially smaller, grains are growing with respect to the out of plane direction, whereas within grains no significant roughness evolution due to plastic deformation can be seen with a pronounced the uprise next to grain boundaries occurs. Regarding the topographical

evolution, Profile 1 highlights the roughening of an approximately (111)/(115) oriented, twinned grain. The two superimposed profile sections, set to a reference point, indicate that the small grain is shrinking in size and at the same time the height in the out of plane direction increased by more than a factor of two after 3500 cycles. From the two AFM images (Fig. 8c, d) it can be seen that the shape has changed from an elongated grain to a circular shaped grain. Profile 2 represents the further uprise of two small, twinned grains. It can be seen that both grains are also growing in the lateral directions. The shape of the two hillock-like grains suggest that surface diffusional mass transport is still somewhat restricted, since significant gradients develop with respect to the lateral height variation of the surface topography. Regarding the microstructural development, the internal twin boundary length is growing although significant changes in the size of certain domains cannot be seen. In certain microstructural features, indicated by Features 1, 2 and 3 (Fig. 8b), advanced damage within the grains can be revealed. Gradual changes of crystal orientation can be seen (Feature 3) leading to an equilibrium configuration of the dislocation network, forming small angle grain boundaries in the red twin lamellae (Features 1, 2). Further details for such small angle grain boundaries will be shown in Fig. 9. The cross-section (Fig. 8g, h) reveals that after 3500 thermo-mechanical loading cycles voids have formed. In Fig. 8h it can be seen that pores reach a size up to the micrometer region and new, small pores also form in the material. These pores lie directly next to an out of plane grown grain, which could indicate that copper atoms were transported to this particular grain, leaving voids.

The progressed cycling state of Film B is presented in Fig. 9. The microstructural evolution is characterized between 1500 (Fig. 9a, c) and 3500 cycles (Fig. 9b, d) using EBSD and AFM sections with a size of $30 \times 30 \mu\text{m}^2$. Comparing Fig. 9a and b no significant changes regarding the twin boundary length is observed, in agreement with Fig. 4b, suggesting that the grains have reached an equilibrium

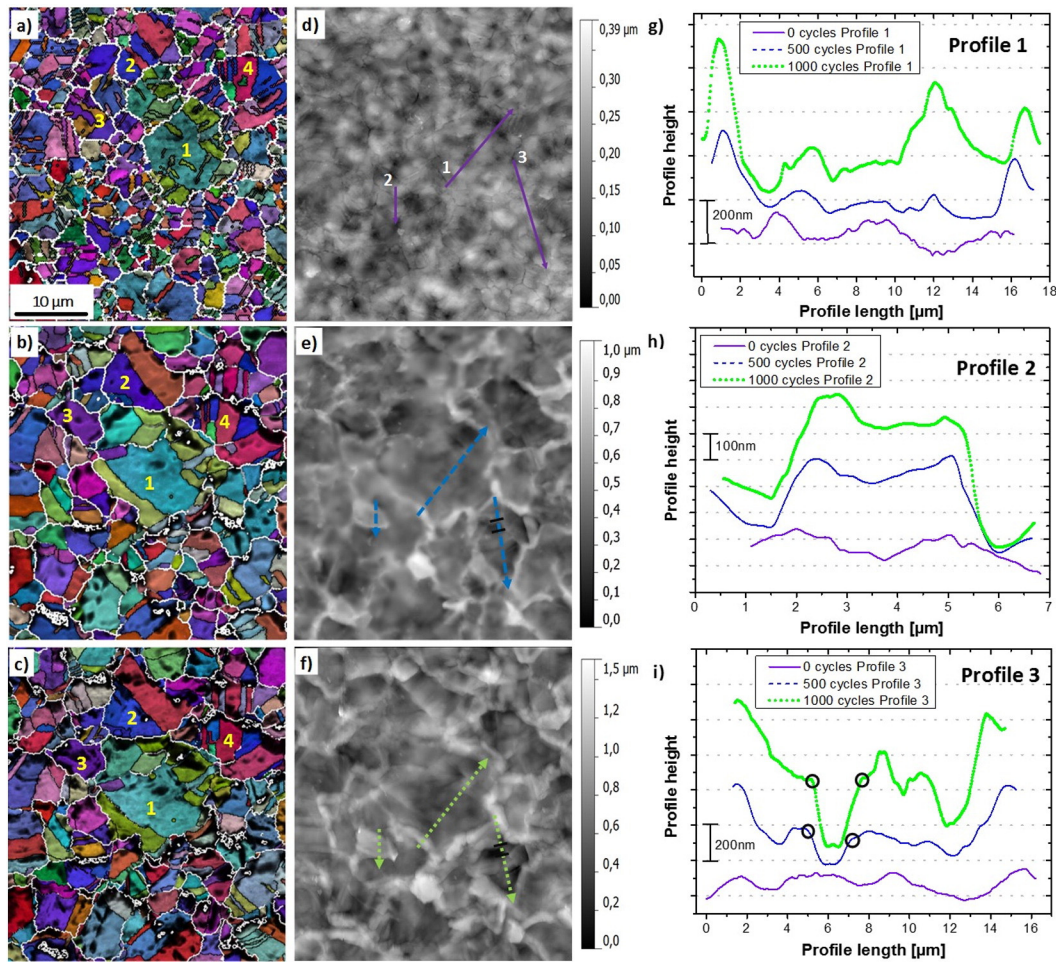


Fig. 7. Early site specific microstructural evolution of Film B. Crystallographic evolution (a–c) is matched by the topographical evolution (d–f) of the same surface area for 0, 500 and 1000 cycles. Three selected microstructural features are examined regarding their topographical evolution, indicated by Profile 1–3 (g–i).

state. Some features remained unchanged, displaying a stable configuration (see Feature 2).

In Feature 1, the (113)-oriented twin, the crystal orientation gradually changes after 3500 cycles (Fig. 9b), whereas for 1500 cycles (Fig. 9a) a constant orientation is observed. A better illustration for such a substructure, evolving in coherent crystal segments (e.g. twins), can be identified in the circular marked (100)-oriented twin segment. After 1500 cycles, the twin segment reveals a colour gradient, indicating that the orientation of the crystal segment is gradually changing. After 3500 cycles a triple junction of three small angle grain boundaries is formed. For a better illustration, Fig. 9g shows the triple junction using a magnified kernel average misorientation image. Thereby, a local misorientation value of the kernel is assigned with respect to the center of the kernel, indicating the small angle grain boundaries as sharp green lines correspond to a mean misorientation angle of about 4° . The dislocations, driven by the applied in-plane stress field, align in an equilibrium configuration forming such 120° segments. This special triple junction angle can be experimentally identified since half of a hexagon has formed, indicating that a polygonisation process is happening. Regarding the film thickness changes of Film B, Figs. 9h and i show a film cross section after 3500 cycles. No pores are visible, even in the magnified image (Fig. 9i). Rather, good interfacial integrity between boundaries can be observed. The overview image also reveals that the twins in Film B have been significantly reduced, resulting in a more columnar grain structure with less intersecting grains through the film thickness. The cross section also confirms the significant surface roughening, which reveals a change in film thickness with respect to the lateral dimensions.

Regarding the topographical changes in the later cycling stage, Profiles 1 and 2 indicate the on-going surface roughening process. In both examples, significant changes due to mass transport on the free surface lead to changes in topography, giving rise to the assumption that in Film B atoms could more easily diffuse to other places.

5. Discussion

The presented results in the previous section show that the thermo-mechanical fatigue behaviour for Film A and Film B differ significantly. While they are nominally similar with respect to the initial microstructure, they reveal a very different thermo-mechanical fatigue behaviour. Summarizing the presented results, three main differences in the fatigue evolution between Films A and B are noted:

- (1) the roughness evolution,
- (2) the microstructural evolution, related to twin boundary migration, grain growth and texture development, and
- (3) the higher driving force for void formation.

Fig. 10 schematically highlights the microstructural differences between Film A and B, which develop during the thermo-mechanical loading process and will be discussed in the following paragraphs. It can be seen that Film A develops a constrained surface roughness (1) which progresses at highly localized HAGB. In the case of Film B such observations were not found, since the roughness evolution was over the entire film surface. Regarding the microstructural evolution, Film A exhibited a very restricted behaviour, where no significant

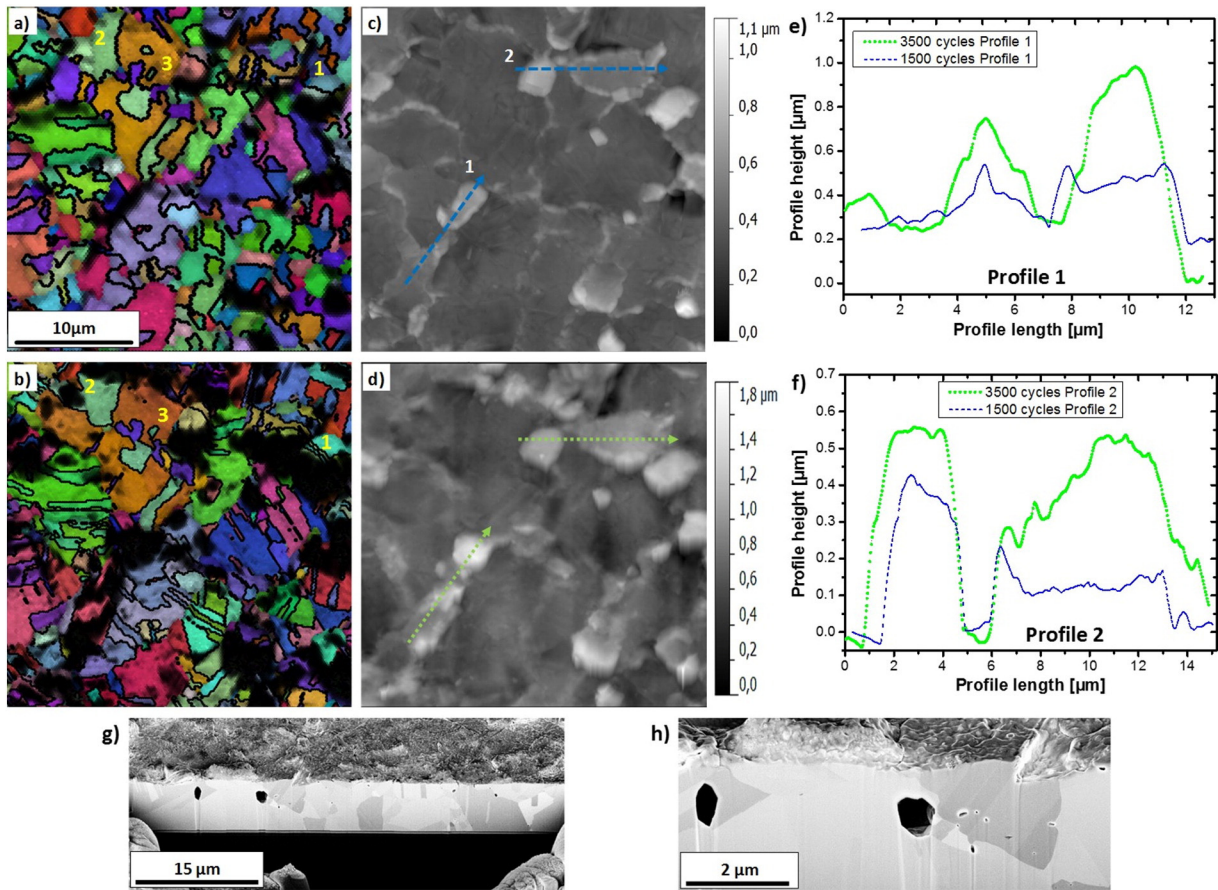


Fig. 8. Film A, site specific microstructural and topographical comparison between 1500 (a, c) and 3500 cycles (b, d) of a $30 \times 30 \mu\text{m}$ surface section. Two profiles indicate topographical changes (e, f) and film cross sections reveal microstructural changes after 3500 cycles (g, h). For 1500 cycles an EBSD scan resolution of $0.3 \mu\text{m}$ was used, after for 3500 cycles the scan was performed with a resolution of $0.2 \mu\text{m}$.

grain growth (2a) or twin boundary migration (2b) were observed. On the contrary, Film B exhibited significant grain growth with continuous reduction of twin boundaries achieved by twin boundary migration. With respect to the void formation potential (3), voids in the micrometer range formed in Film A and no voids were found in Film B regardless of the local microstructural conditions.

Before discussing these aspects in more detail, first the literature status regarding impurity effects in Cu films will be summarized. Previous time-of-flight secondary ion mass spectroscopy (ToF-SIMS) profiles revealed that the most important distinction between the two copper films is that Film A has a significantly higher sulphur and chlorine residual concentration than Film B [7]. Although ToF-SIMS measurements were used in this previous study to determine the impurity levels, quantification is not possible as the sputter yield of different atoms varies and only a relative comparison of the signal intensities is possible after normalizing the values to the copper signal. This relative comparison indicates that Film A has a significantly higher impurity concentration. Quantitative analysis, using XRF measurements revealed that the Cl and S contamination (Film A) is in the ppm range. Hence, it can be stated that both film system contain S and Cl as the main inorganic components, although Film A has a significantly higher concentration and Film B can be seen as a relatively pure copper film. This allows for the discussion on the observed differences in the fatigue evolution of the two copper films with respect to the influence of inorganic impurities.

The initial microstructure already indicates the fundamental difference between Films A and B, where Film A has a 26% higher fractional twin boundary length per unit area than Film B, which is qualitatively indicated by EBSD surface and cross section microstructures (Fig. 2). The fact that Film A has a higher twin density is most likely due to the

fact that for the deposition process a different additive package was used compared to Film B. The main question is what role the significantly higher remaining S and Cl quantities play regarding twin nucleation/stability and subsequent twin densities. Studies propose that incorporated impurities enhance the formation of twins and leading to higher twin densities [31]. It was suggested that modifying elements (Sr, Na), with similar impurity levels (60 ppm), are adsorbed on the solid-liquid interface of the growing crystal, promoting twin formation due to errors in the stacking sequence. This can be seen as impurity induced twinning, where interstitial atoms lower the stacking fault energy of the crystal. For electrochemical copper deposition similar results were obtained, where the increasing additive concentration resulted in a smaller grain size [32]. For electrodeposited copper, it was also observed that the implantation of gallium ions (using FIB) near the surface, right after electrochemical copper deposition, prevented recrystallization processes. This phenomenon can be directly related to the implanted impurity atoms, since copper layer underneath was not affected, hence completely recrystallizing [6].

This preventing effect is also indicated in the film stress evolution (Fig. 3), where Film A showed no changes after 80 thermal cycles, whereas Film B exhibited significant changes. This can be observed in the significant change of the thermo-elastic slope in Film B, going from $-2.09 \text{ MPa}/^\circ\text{C}$ to $-2.51 \text{ MPa}/^\circ\text{C}$ after 80 thermal cycles and approaching the elastic behaviour of Film A. The lower elastic slope in the first cycles of the pure copper Film B might occur due to microplasticity and the film displays a thermo-elastic behaviour on the global scale. At the same time, some local regions in the microstructure plastically deform under the applied stress and temperature. This is in agreement with the significant increase of the grain size and diminishing

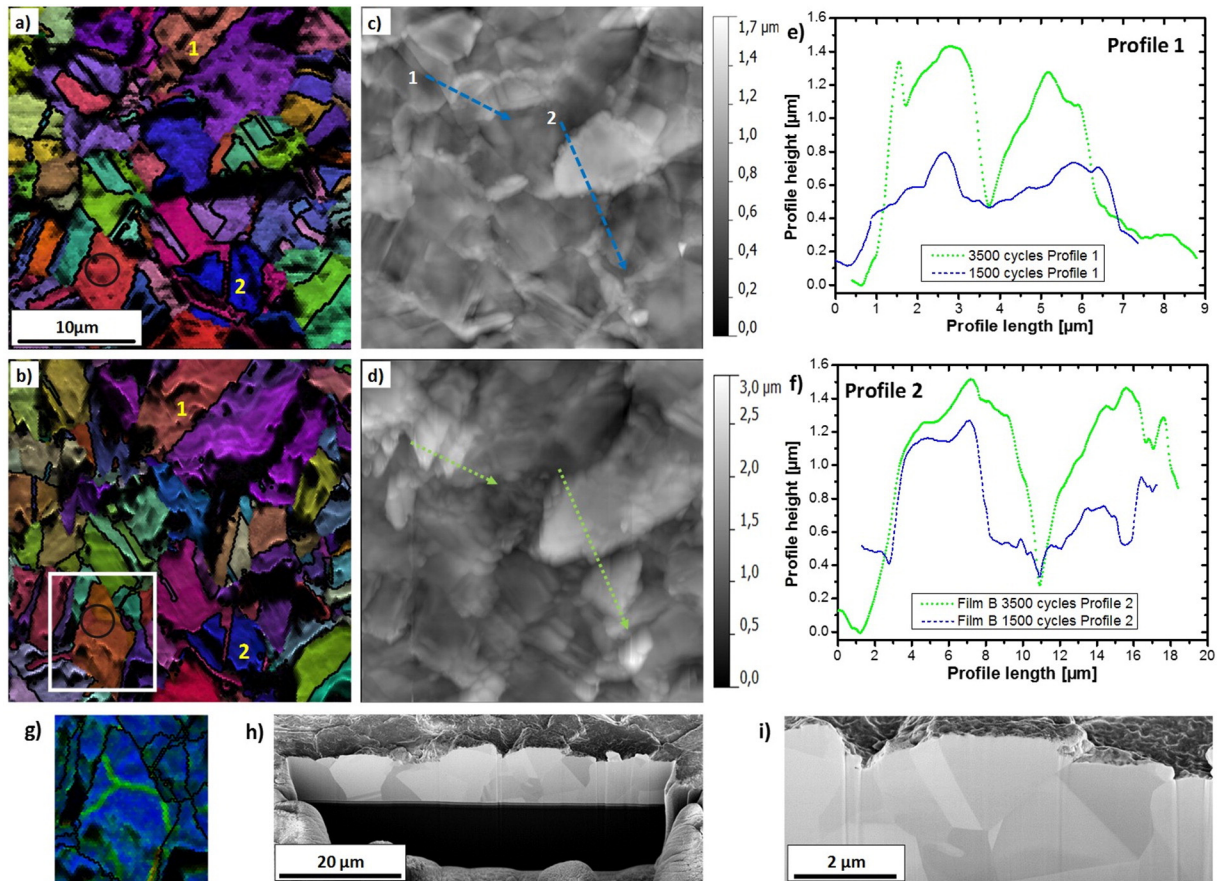


Fig. 9. Film B site specific microstructural and topographical comparison between 1500 (a, c) and 3500 cycles (b, d) of a $30 \times 30 \mu\text{m}$ surface section. A magnified section (g) shows a formed small angle triple junction in a (100) oriented grain. Two profiles indicate topographical changes (e, f) and film cross sections reveal microstructural changes after 3500 cycles (h, i). Due to the on-going surface roughening process, only twin boundaries are indicated.

twin boundary length in the first 100 cycles, revealed by the global microstructural data (Fig. 4). Furthermore, Film A exhibited a higher strength and greater elastic regime, indicating a potential benefit regarding the mechanical properties due to impurities pinning boundaries.

The surface morphology changes (1) show that Film A displays a very pronounced film surface structure. Both, HAGB and twin boundaries exhibit strong grooving (Fig. 5a, d) while the inner surface of the grains remain perfectly flat. In Film B, HAGB can also be identified by grooves at the interface (Fig. 7a, d), but the strong grooving at twin boundary interfaces was not observed. This observation is intriguing since the grooves are normally attributed to the local energy equilibrium of HAGB [33]. The morphology (depth, contact angle, etc.) of the developed grain boundary groove provide qualitative information on

how much the free energy, G , is lowered by the minimization of the grain boundary energy, γ_g along with the rise of the surface energy, γ_s [34]. A strong decrease of interfacial energy is often related to the presence of impurities, because such interstitial atoms bond to the matrix element and lower the energy at the free surface [35, 36]. In the case of Film A, the microstructural investigations indicated that the sulphur and chlorine species are not only found at HAGB [7], but also segregate to twin boundaries significantly modifying their morphology. The subsequent thermo-mechanical loading resulted in a constrained surface roughness evolution for Film A. It appears that segregated impurities modify diffusional processes at the surface, leading to the localized roughening at boundaries. The purer Cu-film, Film B exhibited a consistent roughness evolution over the entire cycling

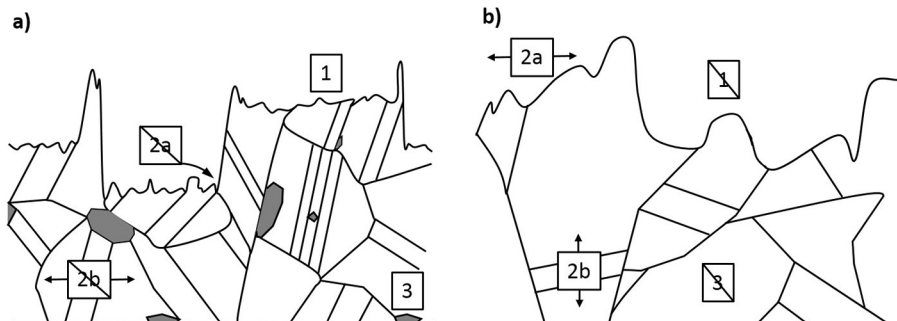


Fig. 10. Schematic microstructural evolution of Film A (a) and Film B (b). Differences can be addressed in the constrained surface roughness evolution for Film A (1), present grain growth (2a) and twin boundary migration (2b) in Film B and the formation of voids (3) in Film A.

experiment, indicating that diffusional processes at the surface are not hindered.

The differences of Film A and B with respect to the microstructural evolution (2) further emphasize the influence of impurities on the thermal fatigue behaviour of Cu films. The pure copper film, Film B, reveals significant grain growth which is going along with the constant diminishing of fractional twin boundary length. In comparison, in Film A such grain growth with coupled twin boundary migration was not observed, although many grains had the same parent/twin configuration as in Film B, as well as higher evolving stresses (see Fig. 3). The global data regarding grain size and twin boundaries directly shows that in Film A deformation mechanisms have to act differently in order to accommodate the applied thermo-mechanical loads achieved by the thermal cycling. Furthermore, the (100)-texture development for Film B clearly shows the increasing occurrence of the (100) crystal orientation, indicating the preferable growth of such grains or twin segments. This is in agreement with basic literature studies where the strong elastic anisotropy in copper provides the driving force with regards to the strain energy minimization. The (100) orientation is energetically preferred if films of a certain thickness (greater $\sim 1 \mu\text{m}$) are subjected to relatively large strains [30,37,38]. On the contrary, the impurity containing copper system Film A had hardly any (100)-texture intensity change during the thermo-mechanical fatigue experiment (Fig. 4c), which shows that such an energy minimization process is prevented. The thermo-mechanical fatigue evolution reveals that in the pure Cu film, Film B, the externally applied thermo-mechanical energy is used to minimize the internally stored energy by microstructural mechanisms, such as grain growth, twin boundary migration/annihilation and texture changes, coupled with severe surface roughening. The impurity enriched Film A does not show such mechanisms.

The imposed thermo-mechanical energy and resulting plastic deformation induced new small angle boundaries within formerly coherent regions (twin lamellae) in the progressed stage of fatigue. The evolution of such microstructural features, predominately found in soft (100) oriented twin segments, shows that the dislocations are initially distributed laterally throughout the crystal segment creating a constant misorientation gradient (Fig. 9a). The acting in-plane stresses caused by further cycling drive the dislocations into an equilibrium structure (hexagonal arrangement of LAGB). This polygonisation is well known in material science since it displays the minimum energy for grains and balances the surfaces tension [39]. Surprisingly the same structure is achieved by the arrangement of dislocations, minimizing their energy with regard to other dislocations, which originates from the elastic stress field of dislocations [40]. Hence, formation of new grain structures, achieved by thermal cycling, revealing a further microstructural fatigue mechanism.

Regarding the void formation potential (3), the film cross-sections for Film A (Fig. 8g, h) revealed that after 3500 cycles voids were found. Furthermore, it appears that the voids seem to be situated underneath distinct upraised grains indicating that atoms come from the inside of the Cu film. Such fatigue features are well known from thermally treated copper–tin solder joints in the microelectronics industry due to the Kirkendall effect [41]. In the case of electroplated copper films previous studies suggest that stress induced void formation occurs due to the misorientation angle between neighbouring grains [42], or due to high stress concentration between twin boundary interfaces and the increased copper diffusivity along grain boundaries [43]. If these models, both based on the concept of stress migration, are used concerning the purer Cu sample type, Film B, one can see that this is not applicable as voids do not form. Voids did not form at HAGB interfaces (Fig. 9h), nor did voids nucleate at the section of dense twin boundary network (Fig. 9i) in the film. The direct comparison of the two Cu films with respect to void formation suggests that the higher S and Cl residual concentration in Film A lowers the free energy for void nucleation, thus promoting the formation of voids inside the copper film. This has also been discussed in other works, specifically dealing

with the relationship between void formation in Cu metallizations and the impurity content [44,45]. Such voids develop when the free energy barrier for void formation:

$$\Delta G = \frac{4\gamma_i^3 f_v}{\sigma^2} \quad (2)$$

is low enough. In Eq. (2), γ_i is the interfacial energy, f_v is a geometrical factor of the void and σ is the local applied stress [46]. A reduced γ_i caused by impurities would significantly promote the void nucleation since γ_i scales to the power of three. The obtained results are also in agreement with other experimental and theoretical observations [47]. The presence of S impurities in Cu leads to a high concentration of excess vacancies in the material, due to the high affinity of the formation of a S-vacancy complex and the segregation of S at grain boundaries along with the energetically favourable formation of Cu_2S . This indicates that for stress induced voiding, impurities significantly alter the void formation potential, as well as revealing that pure copper films are very resistant to voiding.

6. Conclusions and summary

In this work, the thermo-mechanical fatigue behaviour of two different electrodeposited copper film systems was examined. The microstructural evolution was quantitatively and qualitatively analysed via a site-specific tracking technique enabling the investigation of global parameters, as well as certain localized microstructural features. The fatigue behaviour of Cu films was analysed with respect to the influence of inorganic impurities (mostly Cl, S), which are inevitably incorporated by the electrodeposition process of copper metallizations.

In direct comparison, the fatigue behaviour of a Cu-film with inorganic impurities (Cl, S) in the ppm region with similar initial microstructural parameters showed an altered fatigue behaviour. The microstructure of Film A exhibited insignificant grain growth with stable twins. A constrained roughness evolution was observed, indicating that diffusional processes at the film surface occurred in a restricted manner. Moreover, the impurity enriched Cu-film, Film A showed void formation within the film material. The higher film strength and the greater microstructural stability in Film A show that deliberate doping would result also in improvement of certain mechanical properties.

The significantly purer Cu-film, Film B, exhibited pronounced twin boundary migration as a main deformation mechanism along with grain growth. This occurred with continuous roughening of the film surface as well as an increase of the (100) texture throughout the thermo-mechanical loading process. The results revealed that the material response for Film B after the application of a cyclic thermo-mechanical load is linked to energy minimizing processes. Furthermore, the experimental results showed that in the progressed state, where dislocations in coherent crystals form new small angle grain boundaries in a hexagonal arrangement.

Acknowledgement

The work was performed in the project EPPL (Enhanced Power Pilot Line), financially supported by grants from Austria, Germany, The Netherlands, France, Italy, Portugal, and the ENIAC Joint Undertaking (ENIAC JU Grant Agreement no. 325608). This project is co-funded within the programme “Forschung, Innovation und Technologie für Informationstechnologie” by the Austrian Ministry for Transport, Innovation and Technology (project number 838774).

References

- [1] J.C. Anderson, Applications of thin films in microelectronics, *Thin Solid Films* 12 (1972) 1–15.
- [2] W.D. Nix, Mechanical properties of thin films, *Metal. Trans. A* 20 (1989) 2217–2245.

- [3] M. Nelhiebel, R. Illing, C. Schreiber, S. Wöhlert, S. Lanzerstorfer, M. Ladurner, C. Kadow, S. Decker, D. Dibra, H. Unterwalcher, M. Rogalli, W. Robl, T. Herzig, M. Poschgan, M. Inselsbacher, M. Glavanovics, S. Fraissé, A reliable technology concept for active power cycling to extreme temperatures, *Microelectron. Reliab.* 51 (2011) 1927–1932.
- [4] W. Robl, M. Melz, B. Weidgans, R. Hofmann, M. Stecher, Last metal copper metallization for power devices, *IEEE Trans. Semicond. Manuf.* 21 (2008) 358–362.
- [5] R. Vinci, E. Zielinski, J. Bravman, Thermal strain and stress in copper thin films, *Thin Solid Films* 262 (1995) 142–153.
- [6] M. Stangl, Charakterisierung und Optimierung elektrochemisch abgeschiedener Kupferdünnschichtmetallisierungen für Leitbahnen höchstintegrierter Schaltkreise DOI 2007.
- [7] A. Wimmer, M. Smolka, W. Heinz, T. Detzel, W. Robl, C. Motz, V. Eyert, E. Wimmer, F. Jahnel, R. Treichler, G. Dehm, Temperature dependent transition of intragranular plastic to intergranular brittle failure in electrodeposited Cu micro-tensile samples, *Mater. Sci. Eng. A* 618 (2014) 398–405.
- [8] A. Wimmer, W. Heinz, T. Detzel, W. Robl, M. Nellesen, C. Kirchlechner, G. Dehm, Cyclic bending experiments on free-standing Cu micron lines observed by electron backscatter diffraction, *Acta Mater.* 83 (2015) 460–469.
- [9] P.A. Flinn, Measurement and interpretation of stress in copper films as a function of thermal history, *J. Mater. Res.* 6 (1991) 1498–1501.
- [10] M.D. Thouless, J. Gupta, J.M.E. Harper, Stress development and relaxation in copper films during thermal cycling, *J. Mater. Res.* 8 (1993) 1845–1852.
- [11] G.P. Zhang, R. Moenig, Y.B. Park, C.A. Volkert, Thermal fatigue failure analysis of copper interconnects under alternating currents, *Electronic Packaging Technology, 2005 6th International Conference on 2005*, pp. 1–4.
- [12] M. Aicheler, S. Sgobba, G. Arnau-Izquierdo, M. Tadorelli, S. Calatroni, H. Neupert, W. Wuensch, Evolution of surface topography in dependence on the grain orientation during surface thermal fatigue of polycrystalline copper, *Int. J. Fatigue* 33 (2011) 396–402.
- [13] R. Mönig, R. Keller, C. Volkert, Thermal fatigue testing of thin metal films, *Rev. Sci. Instrum.* 75 (2004) 4997–5004.
- [14] O. Kraft, P. Wellner, M. Hommel, R. Schwaiger, E. Arzt, Fatigue behavior of polycrystalline thin copper films, *Z. Met.* 93 (2002) 392–400.
- [15] R. Schwaiger, G. Dehm, O. Kraft, Cyclic deformation of polycrystalline Cu films, *Philos. Mag.* 83 (2003) 693–710.
- [16] R. Keller, J. Phelps, D. Read, Tensile and fracture behavior of free-standing copper films, *Mater. Sci. Eng. A* 214 (1996) 42–52.
- [17] O. Kraft, R. Schwaiger, P. Wellner, Fatigue in thin films: lifetime and damage formation, *Mater. Sci. Eng. A* 319 (2001) 919–923.
- [18] A. Wimmer, A. Leitner, T. Detzel, W. Robl, W. Heinz, R. Pippan, G. Dehm, Damage evolution during cyclic tension–tension loading of micron-sized Cu lines, *Acta Mater.* 67 (2014) 297–307.
- [19] M. Hommel, O. Kraft, Deformation behavior of thin copper films on deformable substrates, *Acta Mater.* 49 (2001) 3935–3947.
- [20] P.A. Flinn, D.S. Gardner, W.D. Nix, Measurement and interpretation of stress in aluminum-based metallization as a function of thermal history, *IEEE Trans. Electron Devices* 34 (1987) 689–699.
- [21] D.P. Field, B.W. True, T.M. Lillo, J.E. Flinn, Observation of twin boundary migration in copper during deformation, *Mater. Sci. Eng. A* 372 (2004) 173–179.
- [22] S. Bigl, S. Wurster, M.J. Cordill, D. Kiener, Site specific microstructural evolution of thermo-mechanically fatigued copper films, *BHM Berg- Huttenmann. Monatsh.* 160 (2015) 235–239.
- [23] T.A. Hahn, Thermal expansion of copper from 20 to 800 K—standard reference material 736, *J. Appl. Phys.* 41 (1970) 5096–5101.
- [24] C. Swenson, Recommended values for the thermal expansivity of silicon from 0 to 1000 K, *J. Phys. Chem. Ref. Data* 12 (1983) 179–182.
- [25] S. Bigl, W. Heinz, M. Kahn, H. Schoenherr, M.J. Cordill, High-temperature characterization of silicon dioxide films with wafer curvature, *JOM* (2015) 1–6, <http://dx.doi.org/10.1007/s11837-015-1600-8>.
- [26] D. Nečas, P. Klapetek, Gwyddion: an open-source software for SPM data analysis, *Cent. Eur. J. Phys.* 10 (2012) 181–188.
- [27] K. Chavez, D. Hess, A novel method of etching copper oxide using acetic acid, *J. Electrochem. Soc.* 148 (2001) G640–G643.
- [28] H. Ledbetter, E. Naimon, Elastic properties of metals and alloys. II. Copper, *J. Phys. Chem. Ref. Data* 3 (1974) 897–935.
- [29] D.S. Gardner, P.A. Flinn, Mechanical stress as a function of temperature in aluminum films, *IEEE Trans. Electron Devices* 35 (1988) 2160–2169.
- [30] C.V. Thompson, R. Carel, Texture development in polycrystalline thin films, *Mater. Sci. Eng. B* 32 (1995) 211–219.
- [31] S.-Z. Lu, A. Hellawell, The mechanism of silicon modification in aluminum–silicon alloys: impurity induced twinning, *Metall. Trans. A* 18 (1987) 1721–1733.
- [32] M. Stangl, M. Lipták, A. Fletcher, J. Acker, J. Thomas, H. Wendrock, S. Oswald, K. Wetzig, Influence of initial microstructure and impurities on Cu room-temperature recrystallization (self-annealing), *Microelectron. Eng.* 85 (2008) 534–541.
- [33] C.V. Thompson, Grain growth in thin films, *Annu. Rev. Mater. Sci.* 20 (1990) 245–268.
- [34] W.W. Mullins, The effect of thermal grooving on grain boundary motion, *Acta Metall.* 6 (1958) 414–427.
- [35] J.W. Martin, R.D. Doherty, B. Cantor, *Stability of Microstructure in Metallic Systems*, Cambridge University Press, 1997.
- [36] A. Mersmann, *Crystallization Technology Handbook*, CRC Press, 2001.
- [37] R. Carel, C. Thompson, H. Frost, Computer simulation of strain energy effects vs surface and interface energy effects on grain growth in thin films, *Acta Mater.* 44 (1996) 2479–2494.
- [38] C.V. Thompson, R. Carel, Stress and grain growth in thin films, *J. Mech. Phys. Solids* 44 (1996) 657–673.
- [39] A. Bhargava, C. Sharma, *Mechanical Behaviour and Testing of Materials*, PHI Learning Pvt. Ltd., 2011.
- [40] D. Hull, D.J. Bacon, *Introduction to Dislocations*, Pergamon Press Oxford, 1984.
- [41] E. Kirkendall, C. Upthegrove, L. Thomassen, Rates of Diffusion of Copper and Zinc in Alpha Brass, *Trans. AIME* 133 (1939) 186–203.
- [42] J. Nucci, R. Keller, D. Field, Y. Shacham-Diamand, Grain boundary misorientation angles and stress-induced voiding in oxide passivated copper interconnects, *Appl. Phys. Lett.* 70 (1997) 1242–1244.
- [43] A. Sekiguchi, J. Koike, S. Kamiya, M. Saka, K. Maruyama, Void formation by thermal stress concentration at twin interfaces in Cu thin films, *Appl. Phys. Lett.* 79 (2001) 1264–1266.
- [44] M. Stangl, J. Acker, S. Oswald, M. Uhlemann, T. Gemming, S. Baunack, K. Wetzig, Incorporation of sulfur, chlorine, and carbon into electroplated Cu thin films, *Microelectron. Eng.* 84 (2007) 54–59.
- [45] M. Stangl, M. Lipták, J. Acker, V. Hoffmann, S. Baunack, K. Wetzig, Influence of incorporated non-metallic impurities on electromigration in copper damascene interconnect lines, *Thin Solid Films* 517 (2009) 2687–2690.
- [46] J. Yu, J. Kim, Effects of residual S on Kirkendall void formation at Cu/Sn–3.5 Ag solder joints, *Acta Mater.* 56 (2008) 5514–5523.
- [47] P.A. Korzhavyi, I.A. Abrikosov, B. Johansson, Theoretical investigation of sulfur solubility in pure copper and dilute copper-based alloys, *Acta Mater.* 47 (1999) 1417–1424.